An orientational perturbation theory for pure liquid water

Teresa Head-Gordon[a] and Frank H. Stillinger
AT&T Bell Laboratories, Murray Hill, New Jersey 07974

This work develops a statistical mechanical perturbation theory for understanding and quantifying the role of directional hydrogen bonding in pure water at any given temperature or density. A reference fluid has been defined with no orientational preferences, but which reproduces the short-ranged oxygen order as determined by x-ray or neutron diffraction. The orientational anisotropy can be reintroduced by perturbing the reference potential toward a fully coupled water potential; we have developed a new water model, ST4, which provides some noticeable structural improvements over its predecessor, ST2, to provide these anisotropic interactions. Monte Carlo simulations at 25 °C and 1 kg/ℓ mass density have been implemented for various values of the coupling parameter to determine the importance of directed hydrogen bonds at various strengths in dictating energetic and structural features of liquid water. We find that virtually full hydrogen bond strength is required to recover the *basic* structural features of liquid water. We have also evaluated and contrasted the inherent structures (potential energy minima) for the reference fluid and the ST4 model, where we find that hydrogen bonding provides significant structural rigidity to resist vibrational distortion. Furthermore, we show that the ST4 model exhibits bifurcated hydrogen bonds which only occur in local regions of high density, i.e., they are found as tetrahedral network defects. These high density clusters also include tetrahedral oxygen triplets, sometimes linearly hydrogen-bonded, which may well serve as low energy intermediates for flow processes in liquid water.

I. INTRODUCTION

The combination of experiment, analytic theory, and computer simulation have greatly contributed to our understanding of pure liquid water and water solutions,[1] although this knowledge still remains imperfect and incomplete in many aspects. In particular, a comprehensive model of liquid water energetics and structure has remained elusive. This is due to the unusual chemical complexity of an associated liquid like water where many-body effects[2,3] and quantum corrections[3,4] are important, and to the theoretical problems associated with treating disordered condensed phase systems. This paper introduces a formal theoretical framework, augmented by computer simulation, which attempts to overcome some of these difficulties with the hope of advancing our understanding of the structural and energetic properties of pure liquid water and water solutions.

We take the structure of hexagonal ice (I_h) as our conceptual starting point. The structure of I_h can be described as an open network of hydrogen bonded water molecules in which the arrangement of oxygen atoms is highly ordered (isomorphous with the wurzite form of zinc sulfide[5]), but where the hydrogen atoms are disordered; these considerations led to Pauling's calculation of the residual entropy for ice I_h at 0 K.[6] We have taken the position that the natural structural division into ordered oxygens and disordered hydrogens arising in I_h can provide insight into

the liquid state as well. Our approach involves a statistical mechanical perturbation theory defined with respect to an unconventional reference system for liquid water, namely one in which the proper local short-ranged oxygen order is maintained, while the orientational (hydrogen-bonding) components are allowed to rotate freely. The perturbation procedure (with coupling constant λ) involves providing appropriate hindrance for these orientational degrees of freedom until the fully coupled water case is reached,

$$\Phi(\lambda) = (1-\lambda)\Phi_0(\mathbf{r}_1,\mathbf{r}_2,...,\mathbf{r}_N)$$
$$+ \lambda\Phi_1(\mathbf{r}_1,\mathbf{r}_2,...,\mathbf{r}_N,\mathbf{s}_1,\mathbf{s}_2,...,\mathbf{s}_N). \quad (1.1)$$

Φ_0 denotes the isotropic reference potential, $\mathbf{r}_i$ represents the oxygen Cartesian coordinates for molecule i, and Φ_1 is the full water interaction with all orientational degrees of freedom, $\mathbf{s}_i$, present. The perturbation format from an isotropic reference state allows us to examine the extent to which pure water properties, and water solution phenomena such as the hydrophobic effect,[7–10] depend upon the degree of orientational anisotropy as defined by Eq. (1.1), and specifically on the presence of directional hydrogen bonds.

In Sec. II we derive our isotropic reference state, Φ_0, for the perturbation procedure. In Sec. III we introduce a new computational model of fully coupled liquid water, Φ_1, which we refer to as ST4; as the name implies it is a variant of the ST2 water model,[11] and provides noticeable structural improvements over its familiar predecessor. We outline the orientational statistical mechanical perturbation theory for liquid water in Sec. IV; while formal ex-

[a] Current address: Lawrence Berkeley Laboratories, Berkeley, California 94720.

pressions as a function of the perturbation strength have been supplied, the full implementation of the orientational perturbation approach is only feasible with computer simulation. Thus in Sec. V we present the energetic and structural properties evaluated from Monte Carlo[12] simulations using the perturbation potential in Eq. (1.1). Section VI discusses inherent structures[13] for our $\lambda=0.0$ and $\lambda=1.0$ end points, which further distinguishes the role of hydrogen bonding in defining water structure. In this same section we briefly discuss Monte Carlo calculations at 198 K, and the inherent structures derived from them, for the two λ end points of 0.0 and 1.0. We find that the structural features of supercooled water are only mildly dependent on temperature as opposed to the larger effect generated by a change in density.[14] In the final section we provide a discussion of the results presented here and of possible directions for future work.

II. REFERENCE STATE FOR PERTURBATION FORMALISM

The I_h ice structure suggests that a fruitful approach for understanding the orientational attributes of liquid water is to define a reference potential which reproduces the (local) oxygen–oxygen structural order, while eliminating the explicit hydrogen-bonding components. The Ornstein–Zernike (OZ) equation,[15]

$$h(r)=c(r)+\rho \int c(\mathbf{r}-\mathbf{r}')h(\mathbf{r}')d\mathbf{r}' \qquad (2.1)$$

averaged over the orientational degrees of freedom, provides an exact relation between the translationally invariant radial distribution function, $h(r)=g(r)-1$, the direct correlation function, $c(r)$, and the density, ρ. With appropriately chosen closures, the OZ equation provides a relationship between an effective isotropic potential and the pair correlation functions. While the usual application of the OZ equation is to extract the pair correlation function for a given model potential, our objective is to define the potential itself given the pair correlation function. An *ab initio* evaluation of the oxygen pair (or higher) correlation function(s) is not possible at the present time. X-ray[16] and neutron diffraction[17] experiments, however, provide measurements of the HH, OH, and OO partial structure factors. An analysis[18,19] of the two types of experiments indicates that the oxygen–oxygen pair correlation derived from the neutron diffraction data of Soper and Phillips[17] may be the best information available on liquid water structure at 25 °C. The oxygen–oxygen radial distribution function, $g_{OO}(r)$, derived from the neutron diffraction data and depicted in Fig. 1, is the first ingredient for obtaining the isotropic reference potential from Eq. (2.1) (although the procedure outlined in this section is applicable in principle to any pair correlation function of interest).

Next we require a closure for the OZ integral equation in order to obtain an approximation to the isotropic potential which reproduces the oxygen–oxygen pair correlation function. We have considered two closures, the Percus–Yevick (PY) closure[20]
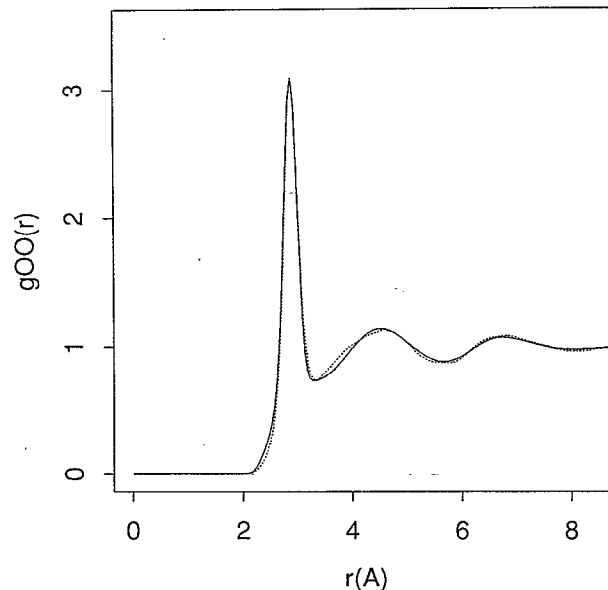

FIG. 1. A comparison of liquid water $g_{OO}(r)$ at 25 °C and 1.0 kg/ℓ derived from neutron diffraction experiments of Soper and Phillips (Ref. 17) (solid line) and that determined from a Monte Carlo simulation (dotted line). As is evident from the figure, the pair correlations are virtually identical, and suggests that the HNC closure provides the correct physics for reproducing the oxygen short-ranged order.

$$\phi(r)=k_bT \ln[1-c(r)/g(r)] \qquad (2.2)$$

and the hypernetted chain (HNC) approximation[15]

$$\phi(r)=k_bT\{g(r)-1-\ln[g(r)]-c(r)\}, \qquad (2.3)$$

where $\phi(r)$ represents a generic pair potential, k_b is Boltzmann's constant, and T is the temperature. The potential functions derived from the OZ equation using the closures defined in Eqs. (2.2) and (2.3) and the Soper–Phillips $g_{OO}(r)$ at 25 °C, are depicted together in Fig. 2. Both show the same qualitative features of a narrow minimum at the oxygen–oxygen distance of 2.86 Å corresponding to oxygens which are directly hydrogen bonded, and broader, more shallow minima at ~4.5 and ~6.2 Å. However there are important quantitative differences between the PY and HNC-derived potentials. In particular, the HNC potential has a more shallow first minimum ($r=2.86$ Å) and is more repulsive at short distances ($r<2.86$ Å) than is the PY-derived potential.

The approximations introduced into the OZ equation with the use of the HNC and PY closures raise the possibility that the potentials appearing in Fig. 2 may not adequately reproduce the experimental $g_{OO}(r)$ in Fig. 1. In fact, we anticipated that interpolation between the PY and HNC approximations might be necessary, or that extrapolation beyond one or the other closure would be required. In order to test the closure approximations, we fitted the PY and HNC data appearing in Fig. 2 to the following functional form:
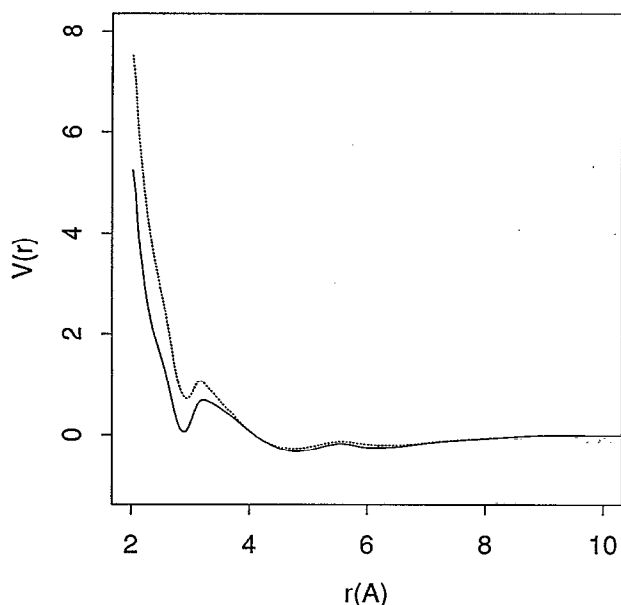
FIG. 2. The potentials derived from the OZ equation using the PY closure (solid line) and the HNC closure (dotted line). Energy and distance units are in kcal/mol and angstroms, respectively. The PY-derived potential did not adequately reproduce the short-ranged oxygen order embodied in $g_{OO}(r)$ in Fig. 1. However, the HNC-derived potential, with no fine tuning, reproduced the short-ranged oxygen order embodied in $g_{OO}(r)$ in Fig. 1 quite well.

$$V_0(r) = \epsilon[(\sigma/r)^a - (\sigma/r)^b]$$

$$+ \sum_{i=1}^{4} h_i \exp[-(r-c_i)^2/w_i^2]. \tag{2.4}$$

The parameters of Eq. (2.4) for the PY and HNC-derived potentials are given in Table I. Given a site–site interaction, we then performed Monte Carlo simulations in order to see whether the experimental pair distribution function is reproduced with the potential under consideration. The Monte Carlo simulation conditions were as follows. The thermodynamic point we have considered is a temperature

TABLE I. Parameters for HNC and PY potentials.[a]

Parameter	HNC	PY
a	9.056	9.648
b	4.044	7.130
ϵ	0.006	0.005
σ	4.218	4.122
c_1	2.849	2.845
c_2	1.514	2.204
c_3	4.569	4.489
c_4	5.518	5.527
w_1	0.253	0.257
w_2	1.767	1.945
w_3	2.363	2.183
w_4	0.614	0.577
h_1	−1.137	−1.132
h_2	3.626	1.664
h_3	−0.451	−0.672
h_4	0.230	0.266

[a]Energy units are kcal/mol.

of 298 K and a density of 0.033 427 7 molecule/Å^3. 216 particles in a cubical cell with periodic boundary conditions were used, and the initial configuration of the system was that of a simple cubic lattice. A step size of 0.025 Å gave a 42% rejection rate, and the pair interaction was truncated at half the box length (~9.3 Å). 5×10^5 Monte Carlo steps were generated to equilibrate the sample, and an additional 5×10^5 steps were run to accumulate the energy and the square of the energy every step, and the radial distribution function statistics every 10 steps.

Figure 1 also displays the radial distribution function derived from the Monte Carlo simulation of the HNC-derived potential; as is evident from the figure, the HNC closure provides a very good approximation to the effective pair interaction which reproduces the local oxygen–oxygen order as defined by the neutron diffraction data. The PY approximation on the other hand performed significantly more poorly. The superior performance of the HNC closure may be due to the neglect of highly connected diagrams, thereby emphasizing the long-ranged correlations over the short-ranged interactions. The neglect of bridge diagrams is often given as the reason why the HNC is thought to be a good closure for integral equation approaches to understanding the structure of polar liquids.[15] The emphasis that the PY closure places on the short-ranged repulsive interactions, inappropriate for an associated liquid such as water, qualitatively accounts for its failure to reproduce the local order in liquid water as defined by the experimental oxygen–oxygen pair correlation function. Thus, we found no need to interpolate between or extrapolate beyond the two closures, but instead find that the HNC-derived potential more than adequately defines the isotropic reference state for the orientational perturbation procedure presented in Secs. V and VII and in the companion paper.[7]

III. THE ST4 WATER POTENTIAL

We have demonstrated that our reference potential ($\lambda = 0.0$), as its definition requires, essentially reproduces the oxygen–oxygen short-ranged order as defined by neutron diffraction studies.[17] At the other extreme $\lambda = 1.0$, many interaction approximations exist for liquid water. Watanabe and Klein (WK) (Ref. 18) recently re-evaluated the structural performance of rigid water models such as TIP4P (Ref. 21) and SPC,[22] and derived a new water potential (the WK model[18]) in light of the new neutron diffraction data.[17] It was concluded that all of the above rigid water potentials did not adequately reproduce the position and/or height of the first peak in the oxygen–oxygen radial distribution function, although all of potentials performed well in describing the second peak.[18]

We then considered the ST2 potential[11] whose "molecular structure" is graphically represented in Fig. 3(a). The functional form of ST2 (Ref. 11) is

$$V_1(1,2) = V_{LJ}(r) + S(r) V_{el}(1,2), \tag{3.1}$$

where r is the distance between water molecule oxygens, V_{LJ} is the standard Lennard-Jones function which depends
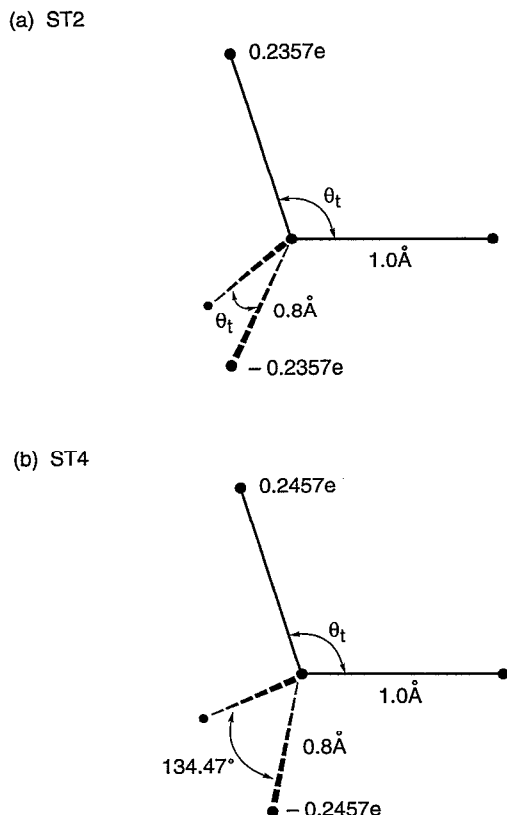
(a) ST2

(b) ST4

FIG. 3. (a) A depiction of the ST2 water model. (b) A depiction of the ST4 water model. θ_t denotes the ideal tetrahedral angle 109.47°.
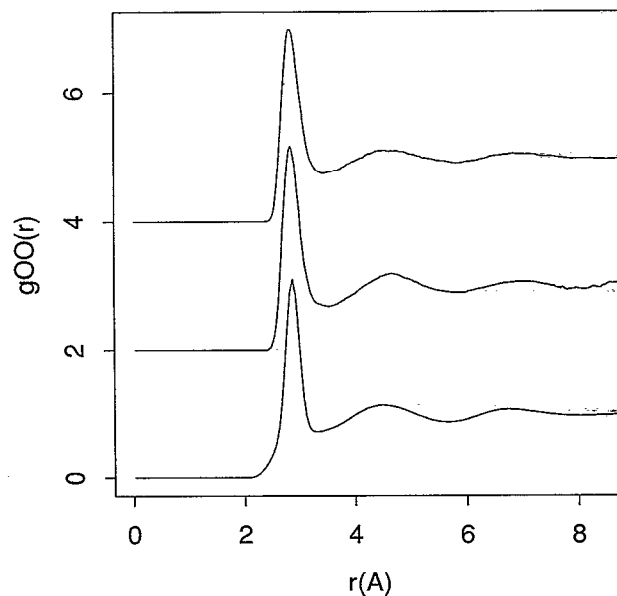

FIG. 4. The radial distribution function, $g_{OO}(r)$, produced from a Monte Carlo simulation at 25 °C and 1.0 kg/ℓ of the ST2 potential (center) and ST4 potential (top) as compared to experiment (bottom). The ST2 potential reproduces the first peak of $g_{OO}(r)$ quite well, but does not exhibit adequate structural agreement at larger values of r. ST4 overcomes this deficiency, in addition to other improvements described in the text.

on the oxygen–oxygen separation only, and V_{el} designates Coulomb's Law evaluated for all sixteen intermolecular charge interactions in the ST2 model. $S(r)$ is a modulating function which interpolates smoothly between 0 and 1, and is applied to the charge interaction in order to avoid electrostatic catastrophes exhibited by some relative orientations of a pair of water molecules,[11]

$$S(r)=0 \qquad 0\leqslant r\leqslant R_L$$

$$S(r)=\frac{(r-R_L)^2(3R_U-R_L-2r)}{(R_U-R_L)^3} \qquad R_L\leqslant r\leqslant R_U \qquad (3.2)$$

$$S(r)=1 \qquad r\geqslant R_U.$$

The ST2 parameters appear in Table II. We evaluated the

TABLE II. Parameters for ST2 and ST4 potentials.

Parameter	ST2	ST4
ϵ (kcal/mol)	0.075 75	0.075 75
σ(Å)	3.100 00	3.100 00
$q_H=-q_L(e)$	0.235 70	0.245 70
r_H(Å)	1.000 00	1.000 00
r_{LP}(Å)	0.800 00	0.800 00
θ_{H-O-H}(°)	109.4700	109.4700
$\theta_{LP-O-LP}$(°)	109.4700	134.4700
R_L(Å)	2.016 00	2.016 00
R_U(Å)	3.128 70	3.128 70

$g_{OO}(r)$, $g_{OH}(r)$, and $g_{HH}(r)$ pair correlation functions for ST2 using Monte Carlo simulation. The conditions were the same as those described in Sec. II for the derivation of the reference potential, except for the following features. The traditional ST2 interaction cutoff of 8.5 Å (Ref. 11) was used, with the interaction truncation being determined solely by the distance between the two oxygens. The list of interactions within the 8.5 Å cutoff was updated every 100 Monte Carlo steps. The initial configuration of the 216 ST2 oxygens was the last configuration generated by the Monte Carlo reference potential calculation described in Sec. II. In the ST2 model, the hydrogen and lone pair positions are rigidly displaced in perfect tetrahedral directions about the oxygen position in the body reference frame [see Fig. 3(a)]. Their positions in the laboratory reference frame are defined by quaternion variables,[23] which are the independent orientational variables. We have chosen to use quaternions in order to avoid the problem with instabilities of the more conventional Euler rotation variables.[23] The initial quaternion values, and thus the hydrogen and lone pair positions, were assigned randomly from a normal distribution. 5×10^5 steps of equilibration and 1×10^6 steps of statistics were evaluated in order to obtain the three pair correlation functions.

Figure 4 shows the comparison of the experimental oxygen–oxygen pair correlation function at 25 °C, and that found from the ST2 simulation. As is evident from the figure, the ST2 potential reproduces the position and height of the first peak extremely well; it unfortunately does not exhibit the correct structure for the second and third peaks. If the second peak is due mostly to configura-
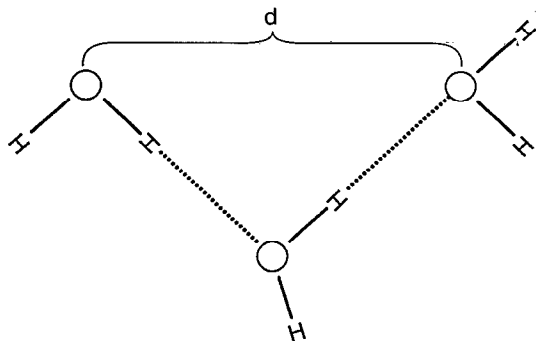
FIG. 5. A representative configuration of three water molecules in liquid water at 25 °C and the experimental density. The distribution of distances, denoted d in this figure, between a central oxygen and the *second* nearest neighbor, define the second peak in $g_{OO}(r)$ (Figs. 1 and 4). By opening up the θ_{LOL} angle of the ST2 model, the average distance $\langle d \rangle$ should diminish, and thus shift the ST2 second peak to smaller r.

FIG. 6. The oxygen–hydrogen correlation, $g_{OH}(r)$, as determined by Monte Carlo simulation at 25 °C and 1.0 kg/ℓ of the ST4 potential (dotted line) and neutron diffraction (solid line) at 25 °C and the experimental density. Overall the agreement is quite good.

tions of three oxygens hydrogen bonded as depicted in Fig. 5, then diminishing the O–O–O angle would shift the ST2 second peak to the desired shorter distances.

In order to improve on the ST2 description of the second and third peaks in the oxygen–oxygen radial distribution function, we introduced a refined ST2 water model which we refer to as ST4 [see Fig. 3(b)]. The ST4 model differs from ST2 in that (1) the charge parameter q_H has been increased from $0.2357e$ to $0.2457e$ ($q_H = -q_L$) and (2) the lone pair-oxygen-lone pair (LP–O–LP) angle has been increased from the ideal tetrahedral value of 109.47° to 134.47° as shown in Fig. 3(b). The reliable reproduction of the position and height of the first peak in $g_{OO}(r)$ is thought to be very sensitive to the repulsive piece of the Lennard-Jones interaction, and largely insensitive to the remaining parameters;[21] we have also found this to be the case. Therefore we have kept the original ST2 ϵ and σ parameters, and the modulation function, S.

The ST4 model improves on the original ST2 model in three ways. First, the new ST4 potential reproduces all of the peak positions and heights of the new diffraction data for the $g_{OO}(r)$ function more adequately than ST2 (and other water models). This was accomplished by increasing the LP–O–LP angle (thereby diminishing the O–O–O angle discussed above). Second, this geometric change improves the quadrupolar description of the condensed phase water model, where an experimental value of $Q_{xx} = 2.63$, $Q_{yy} = -2.50$, $Q_{zz} = -0.13$, in units of 10^{-26} esu cm^2, has been reported.[24] The original ST2 model quadrupole tensor is $Q_{xx} = 1.86$, $Q_{yy} = -1.86$, $Q_{zz} = 0.00$. The symmetry of the fully tetrahedral ST2 model is broken with the opening of the LP–O–LP angle in ST4. In order to maintain an enhanced dipole moment relative to the gas phase (the ST2 model value is 2.35 D), and to obtain the best quadrupole description, the proton charge has been increased, and the lone pair charge decreased, by $0.01e$. These changes result in an ST4 quadrupole tensor of $Q_{xx} = 2.35$, $Q_{yy} = -1.94$, $Q_{zz} = -0.41$, and a dipole moment of 2.1 D. A better quadrupole description is thought to be an important contribution to the dielectric constant,[18,25] although we have not
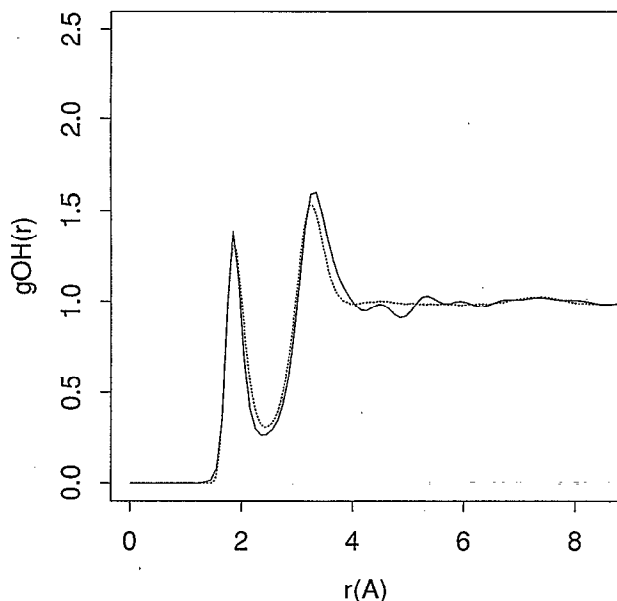
evaluated this quantity for either ST2 or ST4 to see whether this is the case. Lastly, the optimum hydrogen bond energy for the water dimer is -6.57 kcal/mol as compared to the ST2 value of -6.83 kcal/mol, resulting in a lower melting temperature, presumably.

Figure 4 also displays the oxygen–oxygen radial distribution function as determined by a Monte Carlo simulation with the ST4 potential function. The details of the simulation are the same as those given above for ST2. As is clear from Fig. 4, the ST4 potential provides significant improvement in the quality of the simulated $g_{OO}(r)$. A comparison of the first peak position and height between ST2 and ST4 shows that they are virtually identical, indicating that this feature is insensitive to the change in charge and LP–O–LP angle. The second and third peaks have shifted to smaller distances as was desired. Thus we have succeeded in our original goal of reproducing the experimentally observed oxygen short-range order at the $\lambda = 1.0$ end point. In addition to the oxygen–oxygen structural correlations, we provide a comparison of the experimental and simulated ST4 $g_{OH}(r)$ and $g_{HH}(r)$ functions in Figs. 6 and 7. We find quite good structural agreement for $g_{OH}(r)$, but only fair agreement with the experimental $g_{HH}(r)$.

We note that all of the simulations involving electrostatic interactions reported here do not use Ewald sums to account for interactions beyond 8.5 Å. This is both due to historical reasons,[11] and to the fact that the short-ranged structural features of water are known to be insensitive to such long-ranged interactions. While energtic quantities evaluated with a distance cutoff may be suspect, the energetic *trends* discussed below should not change with the introduction of long-ranged interactions. In addition, the
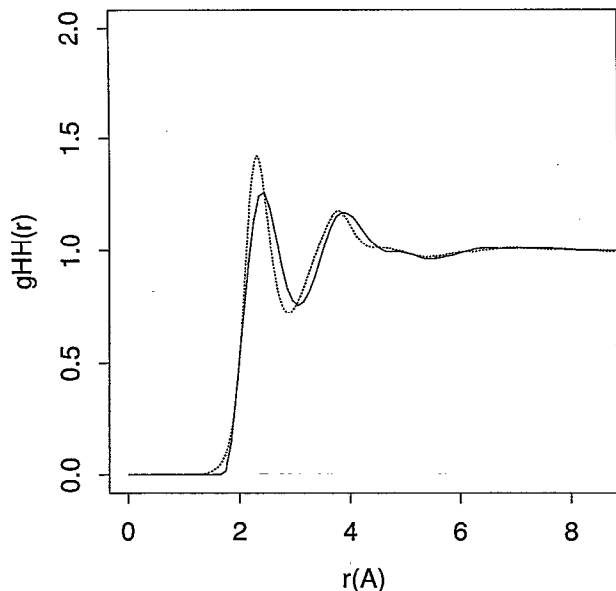
FIG. 7. The hydrogen–hydrogen correlation, $g_{HH}(r)$, as determined by Monte Carlo simulation at 25 °C and 1.0 kg/ℓ of the ST4 potential (dotted line), compared to experiment (solid line). Overall the agreement is only fair.

simulations presented here are purely classical, i.e., no quantum effects have been incorporated into the Monte Carlo simulations. While quantum effects are known to be significant in describing water structure,[4] we justify their exclusion from the calculations presented here on the following grounds. The classical potentials describing the two perturbation end points have been shown to reproduce the structural short-ranged order as described by the (inherently) quantum mechanical neutron diffraction data.[17] In addition, we are evaluating energetic and structural *comparisons* between a reference fluid with no orientational preferences and that which describes pure liquid water, so that cancellation of errors are expected.

IV. ORIENTATIONAL PERTURBATION THEORY FOR LIQUID WATER

Sections II and III outline the functional forms of the reference potential, Φ_0, and the fully coupled potential, Φ_1, introduced in Eq. (1.1); because these potentials are pairwise additive we may rewrite Eq. (1.1) as follows:

$$\Phi(\lambda) = \sum_{i \neq j}^{N} \sum^{N} [(1-\lambda)V_0(r_{ij}) + \lambda V_1(\mathbf{r}_i\mathbf{r}_j\mathbf{s}_i\mathbf{s}_j)]$$

$$= \sum_{i \neq j}^{N} \sum^{N} \{V_0(r_{ij}) + \lambda[V_1(\mathbf{r}_i\mathbf{r}_j\mathbf{s}_i\mathbf{s}_j) - V_0(r_{ij})]\}$$

$$= \sum_{i \neq j}^{N} \sum^{N} [V_0(r_{ij}) + \lambda V_1'(\mathbf{x}_i\mathbf{x}_j)], \qquad (4.1)$$

where $\mathbf{x}_i$ denotes both translational, $\mathbf{r}_i$, and orientational, $\mathbf{s}_i$, degrees of freedom for molecule i. The canonical ensemble

configurational integral as a function of the perturbation parameter λ and the potential energy given in Eq. (4.1) is

$$Z_N(\lambda) = \int d\mathbf{x}_1 \cdots \int d\mathbf{x}_N$$

$$\times \exp\left[-\beta \sum_{i<j}^{N} [V_0(r_{ij}) + \lambda V_1'(\mathbf{x}_i\mathbf{x}_j)]\right] \quad (4.2)$$

which can be reexpressed as the average of $\exp(-\beta\lambda\Sigma_{i<j}^N V_1')$ in the reference ensemble,

$$Z_N(\lambda) = Z_N(0) \left\langle \exp\left[-\beta\lambda \sum_{i<j}^{N} V_1'(\mathbf{x}_i\mathbf{x}_j)\right] \right\rangle_0 . \quad (4.3)$$

If we assume that the effect of $\lambda V_1'$ is small enough to expand in a λ power series, the last expression can be put into the form

$$Z_N(\lambda) = Z_N(0) \exp\left(-\beta\lambda\left\langle \sum_{i<j}^{N} V_1'(\mathbf{x}_i\mathbf{x}_j) \right\rangle_0 \right.$$

$$+ \frac{\beta^2\lambda^2}{2!}\left\{\left\langle \left[\sum_{i<j}^{N} V_1'(\mathbf{x}_i\mathbf{x}_j)\right]^2 \right\rangle_0 \right.$$

$$\left.\left. - \left[\left\langle \sum_{i<j}^{N} V_1'(\mathbf{x}_i\mathbf{x}_j) \right\rangle_0\right]^2\right\} + O(\beta^3\lambda^3)\right).$$

$$(4.4)$$

In principle, the nth order correlation functions $g^{(n)}$ can also be expanded in a power series

$$g^{(n)}(\mathbf{x}_1,...,\mathbf{x}_n,\lambda) = \sum_{l=0}^{\infty} \lambda^l g^{(n,l)}(\mathbf{x}_1,...,\mathbf{x}_n), \qquad (4.5)$$

where the $g^{(n,0)}$ refer to the unperturbed system and so are orientation independent, specifically

$$g^{(n,0)}(\mathbf{x}_1,...,\mathbf{x}_N) = \frac{(8\pi^2 V)^n}{Z_N(0)} \int d\mathbf{x}_{n+1} \cdots \int d\mathbf{x}_N$$

$$\times \exp\left[-\beta \sum_{i<j}^{N} V_0(r_{ij})\right], \qquad (4.6)$$

where V is the system volume. These unperturbed correlation functions permit Eq. (4.4), or equivalently the change in free energy $F_N(\lambda) - F_N(0)$ produced by the perturbation, to be expressed in an alternate fashion

$$\ln[Z_N(\lambda)/Z_N(0)] = -\beta[F_N(\lambda) - F_N(0)] = -\frac{\beta\lambda N(N-1)}{2(8\pi^2 V)^2} \int d\mathbf{x}_1 \int d\mathbf{x}_2 V_1'(\mathbf{x}_1,\mathbf{x}_2) g^{(2,0)}(\mathbf{x}_1,\mathbf{x}_2) + \frac{\beta^2\lambda^2 N(N-1)}{4(8\pi^2 V)^2} \int d\mathbf{x}_1$$

$$\times \int d\mathbf{x}_2 [V_1'(\mathbf{x}_1,\mathbf{x}_2)]^2 g^{(2,0)}(\mathbf{x}_1,\mathbf{x}_2) + \frac{\beta^2\lambda^2 N(N-1)(N-2)}{2(8\pi^2 V)^3} \int d\mathbf{x}_1 \int d\mathbf{x}_2$$

$$\times \int d\mathbf{x}_3 V_1'(\mathbf{x}_1,\mathbf{x}_2) V_1'(\mathbf{x}_1,\mathbf{x}_3) g^{(3,0)}(\mathbf{x}_1,\mathbf{x}_2,\mathbf{x}_3) + \frac{\beta^2\lambda^2 N(N-1)(N-2)(N-3)}{8(8\pi^2 V)^4}$$

$$\times \int d\mathbf{x}_1 \int d\mathbf{x}_2 \int d\mathbf{x}_3 \int d\mathbf{x}_4 V_1'(\mathbf{x}_1,\mathbf{x}_2) V_1'(\mathbf{x}_3,\mathbf{x}_4)$$

$$\times [g^{(4,0)}(\mathbf{x}_1,\mathbf{x}_2,\mathbf{x}_3,\mathbf{x}_4) - g^{(2,0)}(\mathbf{x}_1,\mathbf{x}_2) g^{(2,0)}(\mathbf{x}_3,\mathbf{x}_4)] + \cdots. \qquad (4.7)$$

For completeness we stress that the $g^{(n,1)}$, $l > 0$ can also be expressed in closed form using the unperturbed correlation functions. In particular the linear correction to $g^{(2,0)}$ is

$$g^{(2,1)}(\mathbf{x}_1\mathbf{x}_2) = -\beta V_1'(\mathbf{x}_1,\mathbf{x}_2) g_{OO}^{(2,0)}(\mathbf{x}_1,\mathbf{x}_2) - \frac{(N-2)\beta}{8\pi^2 V} \int d\mathbf{x}_3 [V_1'(\mathbf{x}_1,\mathbf{x}_3) + V_1'(\mathbf{x}_2,\mathbf{x}_3)] g^{(3,0)}(\mathbf{x}_1,\mathbf{x}_2,\mathbf{x}_3)$$

$$-\frac{(N-2)(N-3)\beta}{2(8\pi^2 V)^2} \int d\mathbf{x}_3 \int d\mathbf{x}_4 V_1'(\mathbf{x}_3,\mathbf{x}_4) [g^{(4,0)}(\mathbf{x}_1,\mathbf{x}_2,\mathbf{x}_3,\mathbf{x}_4) - g^{(2,0)}(\mathbf{x}_1,\mathbf{x}_2) g^{(2,0)}(\mathbf{x}_3,\mathbf{x}_4)] + \cdots. \qquad (4.8)$$

It is evident from the expressions in Eqs. (4.7) and (4.8) that quadratic free energy contributions, and linear pair correlation contributions, involve three and four body correlations in the unperturbed ensemble. Since these are very complicated attributes of the system (not easily represented either analytically, tabularly, or graphically), Eqs. (4.7) and (4.8) as presented have rather limited utility. A more useful tactic, followed in Sec. V, is to use direct Monte Carlo simulation for several discrete λ values in the range $0.0 \leqslant \lambda \leqslant 1.0$. If the results are smooth enough to permit simple polynomial fits, the leading-order λ series terms can be inferred indirectly.

We have explicitly evaluated several terms in the statistical mechanical perturbation theory for the binding energy per molecule, since this does not involve higher order structural correlations.

$$\langle\Phi(\lambda)\rangle = \langle V_0(r_{12})\rangle_\lambda + \lambda\langle V_1'(\mathbf{x}_1,\mathbf{x}_2)\rangle_\lambda. \qquad (4.9)$$

As discussed in Sec. II, the reference model interaction was constructed to reproduce the short-ranged oxygen order exhibited by the neutron diffraction experiments (Fig. 1), as was the ST4 water model at the other extreme. If we assume that $g_{OO}(r;\lambda)$ changes very little for intermediate λ values (an assumption to be tested below) then $\langle V_0(r_{12})\rangle_\lambda$ is nearly independent of λ, hence

$$\langle V_0(r_{12})\rangle_\lambda \cong \langle V_0(r_{12})\rangle_0 \qquad (4.10)$$

and the perturbation expression for the binding energy up to second order is

$$\langle\Phi(\lambda)\rangle = \langle V_0(r_{12})\rangle_0 + \lambda\langle V_1'(\mathbf{x}_1,\mathbf{x}_2)\rangle_0$$

$$+ \lambda^2 \left.\frac{\partial\langle V_1'(\mathbf{x}_1,\mathbf{x}_2)\rangle}{\partial\lambda}\right|_{\lambda=0} + O(\lambda^3). \qquad (4.11)$$

The first term in Eq. (4.11) is simply the average binding energy as determined by the $\lambda = 0$ Monte Carlo simulation at 25 °C and the experimental density discussed in Sec. II; we have found the binding energy per particle of our reference fluid to be -2.35 kcal/mol, $\sim 25\%$ of the value expected for the full water interaction.

The terms linear and quadratic terms in λ in Eq. (4.11) involve explicit dependence on the orientational degrees of freedom; because we are evaluating these quantities in the reference ensemble where no orientational dependence is present, we must replace $V_1'(\mathbf{x}_1,\mathbf{x}_2)$ by its average over the orientations of molecules 1 and 2. Most water interactions of the type represented by ST4, ST2, and others of similar ilk,[18,21,22] allow averaging over spherical shells of charge at fixed O–O separation, r_{12}. The integral which arises has the form

$$I(r_{12};l_\alpha,l_\beta) = \frac{2q_1 q_2}{\pi l_\alpha l_\beta r_{12}} \int dk \, \sin(kl_\alpha)\sin(kl_\beta)\sin(kr_{12}), \qquad (4.12)$$

where l_α and l_β represent the lengths of the respective charges from their oxygens. Equation (4.12) is a standard integral whose solution is (for $l_\beta \leqslant l_\alpha$)

$$I(r_{12};l_\alpha,l_\beta) = \frac{1}{l_\alpha} \quad (0 < r_{12} < l_\alpha - l_\beta),$$

$$= \frac{1}{l_\alpha} \left[1 - \frac{(l_\alpha - l_\beta - r_{12})^2}{4 l_\beta r_{12}}\right]$$

$$(l_\alpha - l_\beta < r_{12} < l_\alpha + l_\beta),$$

$$= \frac{1}{r_{12}} \quad (l_\alpha < r_{12}). \qquad (4.13)$$

Hence the linear term in Eq. (4.11) becomes

TABLE III. Binding energy for five values of the perturbation, λ.

λ value	Binding energy (kcal/mol/molecule)
0.00	−2.285
0.25	−2.566
0.50	−4.275
0.75	−6.596
1.00	−9.378

$$\langle V_1'(\mathbf{x}_1,\mathbf{x}_2)\rangle_0 = \rho \int d\mathbf{r}_{12}[V_{LJ}(r_{12}) - V_0(r_{12}) + S(r_{12})]$$

$$\times \sum_{\alpha(1)} \sum_{\beta(2)} q_\alpha q_\beta I(r_{12};l_\alpha,l_\beta)]g_{OO}^{(2,0)}(r_{12}).$$

(4.14)

The sum over charges vanishes on each molecule so that the last term in brackets in Eq. (4.14) vanishes when r_{12} exceeds the maximum of $l_\alpha + l_\beta$. For the model interaction considered in Sec. IV, and others,[18,21,22] this maximum is 2.0 Å. In addition, $g_{OO}(r_{12})$ is zero for distances < 2.0 Å. Therefore the last term in Eq. (4.14) can be dropped altogether to yield the first order correction to the binding energy

$$\langle V_1'(\mathbf{x}_1,\mathbf{x}_2)\rangle_0 = \rho \int d\mathbf{r}_{12}[V_{LJ}(r_{12}) - V_0(r_{12})]g_{OO}^{(2,0)}(r_{12}),$$

(4.15)

The integral appearing in Eq. (4.15) is easily evaluated by numerical quadrature using the experimental radial distribution function; we obtain a value of 3.02 kcal/mol. This positive value indicates that for small perturbations about the $\lambda=0$ point, the slope of $\langle\Phi(\lambda)\rangle$ will be positive, and hence the energy initially rises as the perturbation is turned on. The quadratic term

$$\frac{\partial\langle V_1'(\mathbf{x}_1,\mathbf{x}_2)\rangle}{\partial\lambda}\bigg|_{\lambda=0} = -\beta\{\langle V_1'(\mathbf{x}_1,\mathbf{x}_2)^2\rangle_\lambda$$

$$- [\langle V_1'(\mathbf{x}_1,\mathbf{x}_2)\rangle_\lambda]^2\}$$

(4.16)

is clearly negative indicating initial downward curvature, which is to be expected as the attractive, cohesive hydrogen bond interaction is restored for nonzero λ values.

V. PERTURBATION CALCULATIONS AS A FUNCTION OF THE COUPLING, λ

In addition to the formal perturbation expressions provided in the previous section, we have evaluated properties by Monte Carlo simulation using the potential given in Eq. (1.1) for several values of the linear coupling parameter λ, 0.00, 0.25, 0.50, 0.75, and 1.00. Table III provides the binding energy for the five values of the coupling parameter λ. It is evident that the binding energy is significantly nonlinear in the coupling parameter, as expected from the analytic calculations of this quantity presented in Sec. IV.

Figures 1, 4, and 8, portray the oxygen–oxygen radial distribution function at room temperature and the experimental density as derived from Monte Carlo for the five λ
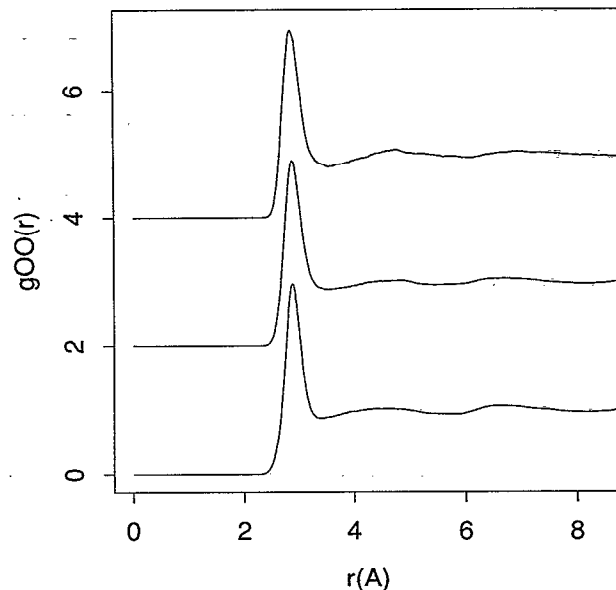

FIG. 8. The oxygen–oxygen structural correlations as determined by Monte Carlo simulation at 25 °C and 1.0 kg/ℓ using the perturbation potential in Eq. (1.1). The perturbation parameter values used to generate the $g_{OO}(r)$'s in this figure are 0.25 (bottom), 0.50 (center), and 0.75 (top). The washed out structure of the second and third peaks at $\lambda=0.25$ and 0.50 is due to frustrated interactions of the $\lambda=0$ and 1 potentials, each of which individually reproduces $g_{OO}(r)$. At $\lambda=0.75$ the directed hydrogen bonding interaction is beginning to dominant, as manifested by the appearance of more well-defined structure than that of $\lambda=0.25$ and 0.50.
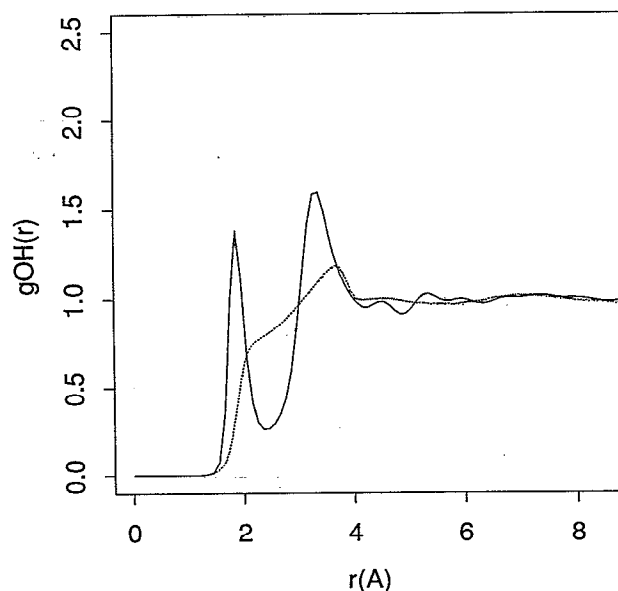

FIG. 9. The oxygen–hydrogen correlation, $g_{OH}(r)$ for $\lambda=0.00$ (dotted line) as determined by Monte Carlo simulation at 25 °C and 1.0 kg/ℓ; the solid line is the experimental $g_{OH}(r)$. This structural correlation is obtained by averaging over all hypothetical hydrogen-bond conformations, and requires $g_{OO}(r)$ from Fig. 1. This figure best represents the properties of our reference potential—a fluid with no obvious orientational preference for hydrogen bonding.
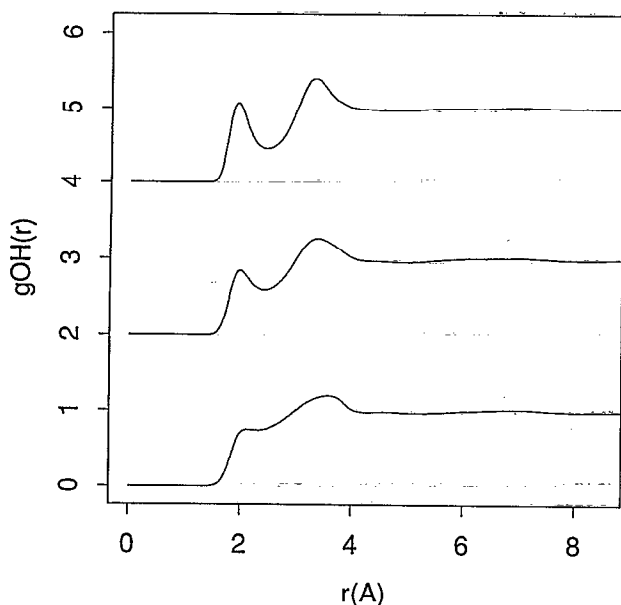
FIG. 10. The oxygen–hydrogen structural correlations as determined by Monte Carlo simulation at 25 °C and 1.0 kg/ℓ using the perturbation potential in Eq. (1.1). The values of the perturbation parameter used to generate the $g_{OH}(r)$'s is 0.25 (bottom), 0.50 (center), and 0.75 (top). This direct probe of hydrogen bonding structure appears to recover linearly as a function of the perturbation.

values. It is evident that the oxygen short-range order is not well reproduced for intermediate values of λ (0.25, 0.50, and 0.75), particularly at the second and third neighbor peaks (see Fig. 8). However the underlying reason for this poor agreement for intermediate values of the coupling is explained by the peculiarities of the correlations of order >2, discussed below.

We also have evaluated the oxygen–hydrogen radial distribution function for the five points sampled in the full λ range (Figs. 6, 9, and 10), including that for $\lambda=0.00$. Given a water molecule O–H bond length of $l=1$ Å, and orientationally averaging over all possible O–H···O angles, we arrive at the expression for $g_{OH}(r)$ for $\lambda=0.00$,

$$g_{OH}(r) = \frac{1}{2lr} \int_{|r-l|}^{r+l} s\, g_{OO}(s)\, ds \qquad (5.1)$$

which was evaluated by numerical quadrature using the oxygen–oxygen pair correlation function. Figure 9, which compares the experimental $g_{OH}(r)$ with that determined at $\lambda=0.00$ using Eq. (5.1), best exemplifies the properties of the reference fluid important for our perturbation approach—the loss of an obvious orientational preference. The structure which does occur is due to the indirect influence of the hydrogen bonding characteristics of water on the oxygen–oxygen structural correlations. The recovery of this orientational profile of hydrogen bonding structure seems to be roughly linear in the perturbation parameter λ, where Fig. 10 displays $g_{OH}(r)$ for the intermediate λ values. Interestingly enough, integration under the first peak of $g_{OH}(r)$, which provides the average number of hydrogen bonds, $\langle N_{HB} \rangle$,

$$\langle N_{HB} \rangle = 4\pi\rho_H \int_0^{r_c} r^2 g_{OH}(r)\, dr \qquad (5.2)$$

($r_c=2.35$ Å) nearly reaches its icelike value of 2 at $\lambda=0.75$, i.e., the full recovery of the average number of hydrogen bonds is not a linear function of the coupling parameter. The values for $\langle N_{HB} \rangle$ we find are 1.39, 1.42, 1.71, 1.96, and 1.98 for increasing λ. This is not inconsistent with the approximately linear recovery of $g_{OH}(r)$ as a function of λ, in that there is a larger spread about the mean in the first (and second) peak for the $\lambda=0.75$ O–H pair correlation function. The large spread is due to incomplete orientational preferences at this intermediate λ value.

Orientational ambiguity is also evident in the calculated mean number of nearest neighbors, $\langle N_O \rangle$, as determined by integration under the first peak of the oxygen–oxygen radial distribution function.

$$\langle N_O \rangle = 4\pi\rho_O \int_0^{r_c} r^2 g_{OO}(r)\, dr, \qquad (5.3)$$

where values of 4.6, 4.9, 5.5, 5.7, and 5.1 are found for increasing λ using a cutoff $r_c=3.36$ Å. The larger average obtained for intermediate λ points is due to a shift in the position of the first trough of $g_{OO}(r)$ to larger r, and to a smaller gradient at r_c as the first minimum in $g_{OO}(r)$ is reached.

Table IV tabulates the nearest-neighbor distribution function for the five λ values simulated at 298 K. The

TABLE IV. Nearest-neighbor distributions.

No. NN	$\lambda=0.00$[a]	$\lambda=0.25$[a]	$\lambda=0.50$[a]	$\lambda=0.75$[a]	$\lambda=1.00$[a]	$\lambda=0.00$[b]	$\lambda=1.00$[b]
0	0.0000	0.0002	0.0002	0.0000	0.0000	0.0000	0.0000
1	0.0028	0.0022	0.0022	0.0008	0.0002	0.0007	0.0000
2	0.0298	0.0263	0.0205	0.0099	0.0056	0.0169	0.0016
3	0.1301	0.1099	0.0986	0.0750	0.0608	0.1091	0.0544
4	0.2923	0.2741	0.2668	0.2702	0.3193	0.2981	0.4407
5	0.3266	0.3202	0.3343	0.3431	0.3417	0.3623	0.3153
6	0.1731	0.1999	0.2021	0.2156	0.1886	0.1793	0.1430
7	0.0407	0.0583	0.0634	0.0704	0.0636	0.0316	0.0404
8	0.0046	0.0084	0.0112	0.0135	0.0095	0.0019	0.0043
9	0.0000	0.0005	0.0007	0.0013	0.0009	0.0000	0.0003
10	0.0000	0.0000	0.0000	0.0001	0.0002	0.0000	0.0001

[a]Evaluated from 298 K simulation configurations.
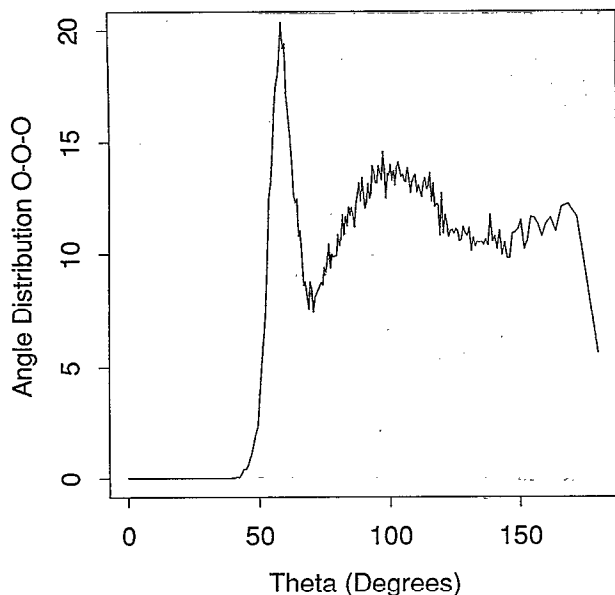[b]Evaluated from 298 K quenched configurations.

FIG. 11. The O–O–O angle distribution function for $\lambda=0.00$. The three-body correlations reveal the reference fluid as a highly defective tetrahedral network due to the prominence of 60° configurations and the unusually large number of near-linear triplets.

distribution is calculated by binning integer numbers of neighbors defined within a radius of 3.36 Å about a central water molecule. Again, orientational indifference seems to be responsible for a wider distribution of nearest neighbors
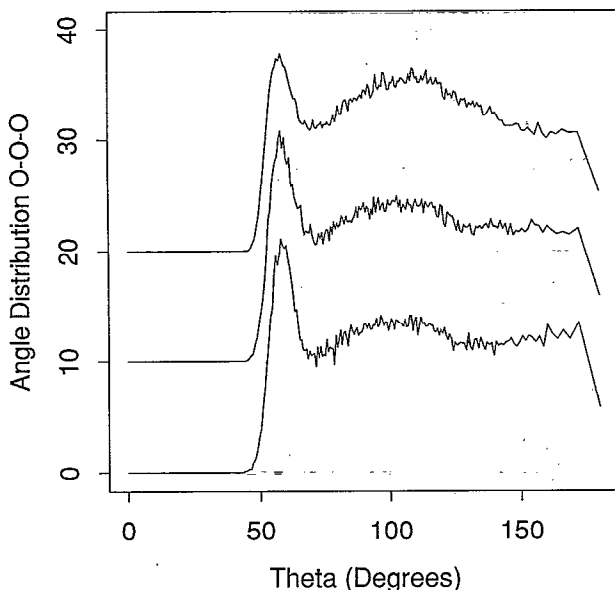

FIG. 12. The O–O–O angle distribution function for $\lambda=0.25$ (bottom), 0.50 (center), and 0.75 (top). Despite the introduction of directional hydrogen bonds, they are evidently too weak at $\lambda=0.25$ and 0.50 to perturb the three-body correlations defined by the reference fluid (Fig. 11). At $\lambda=0.75$, the hydrogen bonding interaction is now of sufficient strength so that a loss of network defects are observed relative to that in Fig. 11; nonetheless, 60° configurations are still the highest maximum.
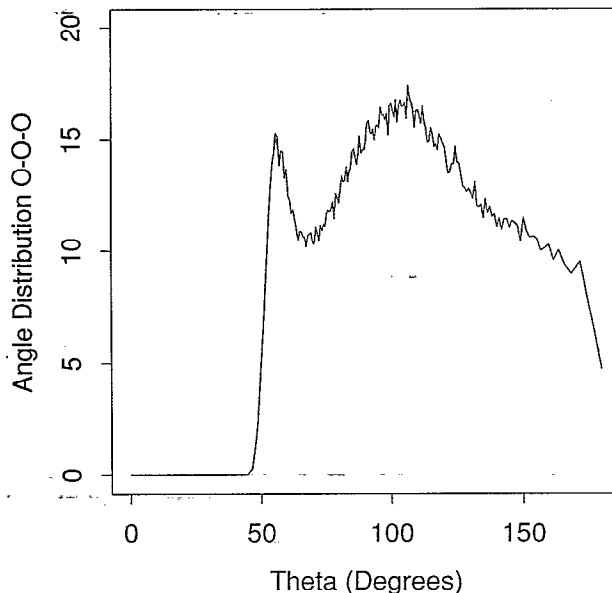
FIG. 13. The O–O–O angle distribution function for $\lambda=1.00$. The full hydrogen bonding interaction is required to make the tetrahedral angle the highest maximum. However, there is still a nontrivial amount of defect structure. The predominance of tetrahedral, linear hydrogen bonding arrangements is consistent with the high boiling point of water, while defects (60° configurations) may provide reasonably low energy intermediates for flow.

in the first coordination shell until a λ value of 0.75 is reached.

The structural ambiguity displayed by the averages and two-body correlations as discussed above can be better understood in terms of the O–O–O angle distribution functions at each of the five λ points, provided in Figs. 11–13. The angle distribution is evaluated by binning the dot product of two vectors emanating from a central oxygen to two of its nearest neighbors, where all possible dot products are considered. Despite the agreement of the two-body correlations at the perturbation coupling parameter endpoints, the three-body correlations (Figs. 11 and 13) at these end points are quite different. In fact for $\lambda=0.00$–0.50 there appear to be many approximately equilateral triangular configurations in contrast to the tetrahedral angle maximum expected for fully coupled water. Only as the hydrogen bond coupling strength increases to (again) 75% of its maximum do the 60° structures begin to diminish. In addition, a shift in the second maximum to the proper tetrahedral value of 109.5° does not occur until the anisotropic coupling reaches 75%. However, the 60° configurations still persist to some extent even in the fully coupled water case. We return to a discussion of these nontetrahedral network defects in the last two sections. Overall, the angle distributions for intermediate λ values (0.25–0.75) are quite broad, especially in the 60°–120° range. The angle distribution functions are quite effective in portraying the potential energy playoff between a highly defective tetrahedral network characterized by the $\lambda=0.00$ reference fluid, and the icelike tetrahedral structure of the fully coupled water case. Since the higher maximum in the angle distribution functions for these two end points are differ-

ent, intermediate λ values sample a wider array of angles between the two angle extremes.

The main conclusion to be drawn from this section is that interaction anisotropy as a property in itself is not as important as the strength of the anisotropy in determining liquid water structure. Evidently the means by which Φ_0 and Φ_1 individually produce proper oxygen pair correlation come into conflict in the intermediate coupling regime, and give rise to frustration. The two- and three-body correlations together provide the following structural picture to support this conclusion. The inexactness in the second and third peaks (and troughs) observed for the pair distribution functions at intermediate λ values is due to the flatter and broader distribution of angles, especially around the 60° and tetrahedral-hydrogen bonded geometry maxima. Clearly the intermediate coupling electrostatic interactions permit partial reorientation and translation from defective equilateral triangle configurations toward those which are close to, but not quite, tetrahedral. The greater number of near-180° configurations, and the breadth of the distribution around this angle, may be a consequence of triangles sharing a vertex, and pivoting about this vertex gives rise to a range of near-linear alignment of three oxygens. Not until close to full hydrogen bonding strength is reached do we see a significant loss of defect (nontetrahedral) structure, and an orientational commitment to the tetrahedral network which characterizes liquid water as we know it.

VI. INHERENT STRUCTURES DETERMINED FROM ROOM TEMPERATURE SIMULATIONS

Inherent structure theory[13] has provided a working foundation for understanding the structural properties of a wide array of liquids. While inherent structure concepts have already been useful for understanding structure in (models of) pure liquid water,[14,26] the inherent structures determined from our perturbation end points ($\lambda=0$ and 1) reveal with much greater clarity the relative roles of directed hydrogen bonds and thermal vibrational deformations in defining observed water structure.

During the course of the Monte Carlo simulations for $\lambda=0$ and 1 described in Secs. II and III, configurations were saved every 10 000 steps for later mapping onto potential energy minima by the method of steepest descents. Properties discussed in this section are based on averages of these 50 inherent structures for each λ end point (inherent structures for $\lambda=1.0$ were evaluated from configurations generated in the second half of the corresponding Monte Carlo simulation).

Figure 14 shows $g_{OO}(r)$ evaluated from the inherent structures and from the 298 K simulation prior to quenching, for $\lambda=0$. The removal of thermal vibrations amplifies the underlying short-ranged order dramatically. In particular, the first peak is sharpened to such an extent that no configurations with pair separations between 3.0 and 3.3 Å are observed. Apparently the narrow, positive energy minimum of the HNC-derived reference potential displayed in Fig. 2 is responsible for trapping particles in order to main-
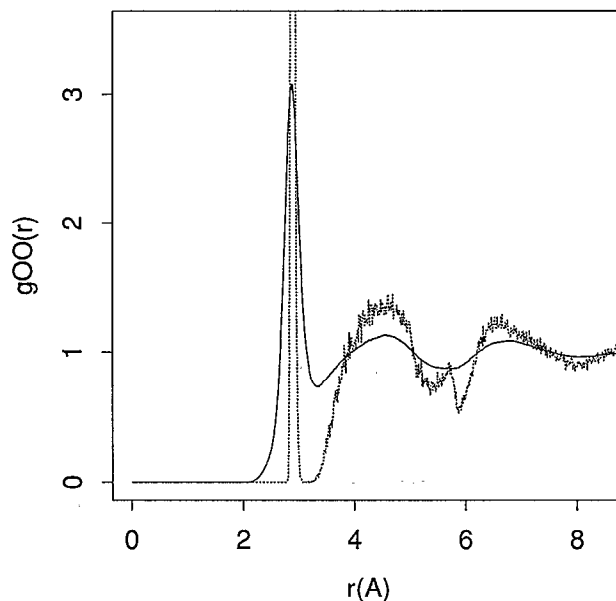

FIG. 14. A comparison of the Monte Carlo simulated $g_{OO}(r)$ of $\lambda=0.00$ at 25 °C and 1.0 kg/ℓ (solid line) and that determined from inherent structure theory for the reference fluid (dotted line). Removal of thermal vibration reveals the first peak of the quenched $g_{OO}(r)$ to be so sharp that no configurations below 55° and between 65° to 70° are observed. Note the unexpected appearance of a peak at 5.7 Å.

tain this aspect of the short-ranged water structure. The second and third peaks are also sharper, but broader than the first, and likely correspond to the shallow minima in $V_0(r)$ at $r=\sim4.5$ and ~6.5 Å, respectively. The unexpected feature at ~5.7 Å in Fig. 14 is also an indirect consequence of the narrow positive energy minimum, and
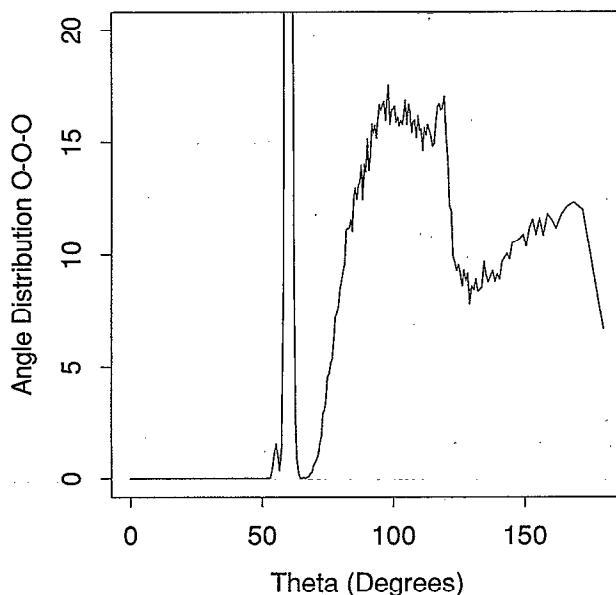

FIG. 15. The O–O–O angle distribution function derived from quenched configurations of the $\lambda=0.00$ reference fluid. The inherent structure procedure best exemplifies the highly defective tetrahedral network of the reference fluid.
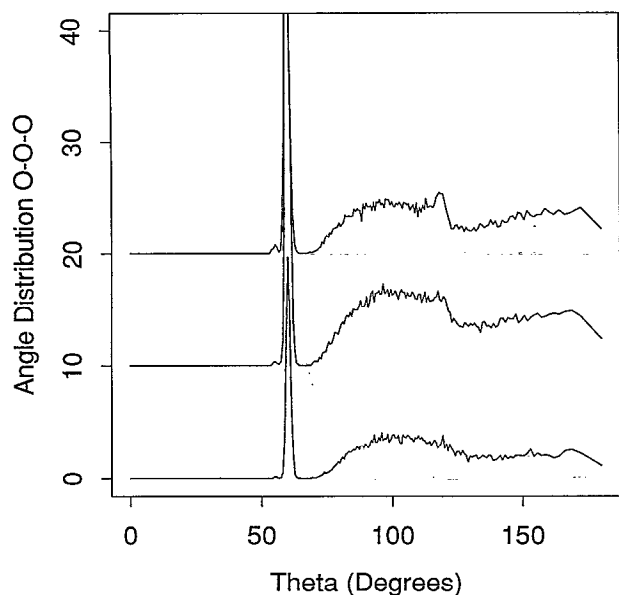
FIG. 16. A breakdown of the O–O–O angle distribution function derived from quenched configurations of the $\lambda=0.00$ reference fluid into the contributions from four (top), five (center), and six (top) nearest neighbors only. While there are equal contributions to tetrahedral structure (109.5°) from four and six nearest neighbors for the $\lambda=0.00$ fluid, the tetrahedral structure arises predominantly from the high density region of five nearest neighbors. In addition, a majority of defect structure (60°) is due to local regions of high density (five or more nearest neighbors).

FIG. 17. A comparison of the Monte Carlo simulated $g_{OO}(r)$ of $\lambda=1.00$ at 25 °C and 1.0 kg/ℓ (solid line) and that determined from inherent structure theory for the fully coupled water case (dotted line). The degree to which vibration contributes to water structure is much smaller than the reference fluid (see Fig. 14). Thus hydrogen bonding interactions "lock-in" structure so that water is less susceptible to vibrational distortion.

its physical explanation will be revealed when we discuss the angle distributions below.

The distribution of nearest neighbors for the quenched $\lambda=0$ configurations is tabulated in Table IV. In contrast to the premapping results (Table IV), the quenched distribution is narrower, while the average number of nearest neighbors shifts from 4.6 to 4.7. Figure 15 shows the angle distribution functions for our reference fluid after potential minimum mapping. Again, this quenching provides a stark portrayal of the short-ranged order now exhibited in the three-body correlations. While the peak at the tetrahedral angle of 109.5° has sharpened somewhat after quenching, the peak at 60° has narrowed so substantially that no sampling of angles below 55° and between 65° and 70° is observed.

The observation of a larger proportion of near linear angles for the $\lambda=0$ reference fluid as compared to the $\lambda=1$ case has already been discussed in Sec. V. The unexpected peak at 5.7 Å alluded to above seems to be a consequence of the higher proportion of equilateral triangular configurations, induced by the first minimum at ~2.85 Å of the reference potential (Fig. 2), where linear arrangements can result when two triangles are joined at one vertex. The breadth of the angular distribution peaks at the tetrahedral and linear angles are presumably structurally inherent, and not a result of thermal broadening, due to the large range of angles available as two triangles pivot about a shared vertex. This structural flexibility is evident in the weakness of the radial distribution function peak at 5.7 Å, and the
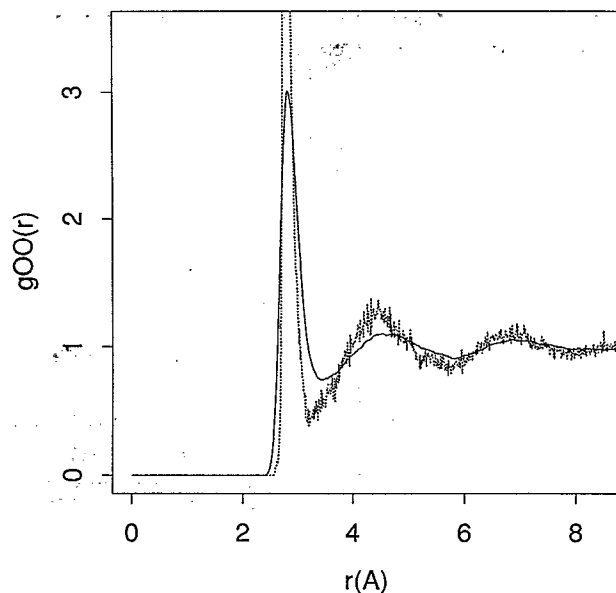
resistance of the tetrahedral and linear angles to sharpen appreciably upon quenching.

The removal of thermal vibration has revealed the reference fluid to be a highly defective tetrahedral network. Figure 16 provides a breakdown of the $\lambda=0$ angle distribution function for O–O–O triplets in the inherent structures into contributions from four, five, and six nearest neighbors, respectively. It is clear from the figure that the equilateral triangular configurations are contributions from high density polyhedral clusters of five and six water molecules in the first solvation shell about a central water molecule. Configurations which we have displayed with molecular graphics show that the underlying structure of the reference fluid exhibits a network of equilateral triangles sharing vertices, edges, and faces, connecting opposite extremes of the periodic cell. While individual triangles, or isolated pairs of triangles sharing a vertex or an edge are observed, all configurations which we have examined by graphics indicate that the $\lambda=0$ fluid is above the percolation threshold in this type of networking.

Next we consider the structural probes generated from the $\lambda=1$ inherent structures. Figure 17 exhibits the quenched $g_{OO}(r)$ for $\lambda=1$ where it is clear that structural features have also sharpened after removal of thermal vibrations. However, the relative change upon quenching is much less dramatic than for the $\lambda=0$ fluid. Figure 18 portrays the angle distribution function where we find that there is now a smaller population of 60° configurations (network defects), and a sharpening of the tetrahedral angle, relative to the prequenched results. The nearest-neighbor distribution tabulated in Table IV is found to be sharper than its prequenched analog, and the mean num-
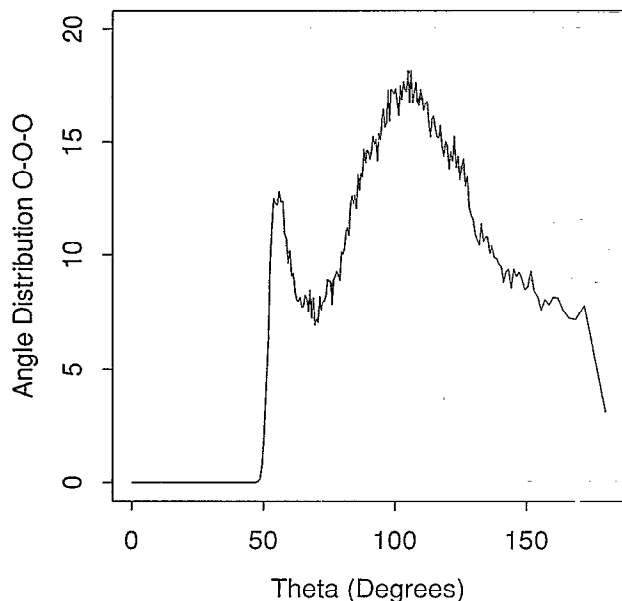
FIG. 18. The O–O–O angle distribution function derived from quenched configurations of the λ=1.00 fully coupled water case. The inherent structures reveal a largely tetrahedral network, with some network defects. Like $g_{OO}(r)$ (Fig. 17), the angle distributions are not subject to much change upon removal of thermal vibrations due to the strong interaction strength of hydrogen bonding which "locks-in" structure.

FIG. 19. A breakdown of the O–O–O angle distribution function derived from quenched configurations of the λ=1.00 case into the contributions from four (bottom), five (center), and six (top) nearest neighbors only. This figure provides direct evidence that for fully coupled water virtually no tetrahedral network defects exist for local water densities of four nearest neighbors. It is evident that local regions of high density incorporate both defect structure and tetrahedral configurations of oxygen triplets, and may serve as low energy intermediates for flow processes.

ber of nearest neighbors has shifted downward from 4.8 to 4.7.

Bearing the λ=0 inherent structure results in mind, the inherent structures derived from the fully coupled water case reveal the structural nature of hydrogen bonding in a new light. First, directional hydrogen bonding provides enough structural rigidity so that fully coupled water is quite resistant to thermal deformation. By contrast, fluids with little or no orientational preference have a great deal of underlying structure which is washed out due to thermal broadening, even for our reference fluid which is "water-like" in some respects. The highly defective network of the reference fluid is still present, albeit to a much smaller extent, in the fully coupled case. A breakdown of the angle distribution into contributions from oxygens with only four, five, and six nearest neighbors (Fig. 19) indicates again that the nontetrahedral defects arise from high density regions where there are five and six neighbors around a central oxygen, although these high density regions contribute to tetrahedral configurations as well. With the full hydrogen bonding interaction present, we provide a visual example of the structure of these local defect clusters in Fig. 20. Again, complex polyhedra providing triangular faces are evident, as well as structures broadly defined about the tetrahedral angle, as triangles share vertices, edges, and faces. We have found by graphical display, and quantified below, that the triangular configurations are stabilized by a diverse set of hydrogen bonding arrangements. Figure 20 shows that these triangular structures arise due to contributions from bifurcated hydrogen bonds (one proton engaged in two hydrogen bonds), as well as nearly linear hydrogen bonds between water molecules whose ox-
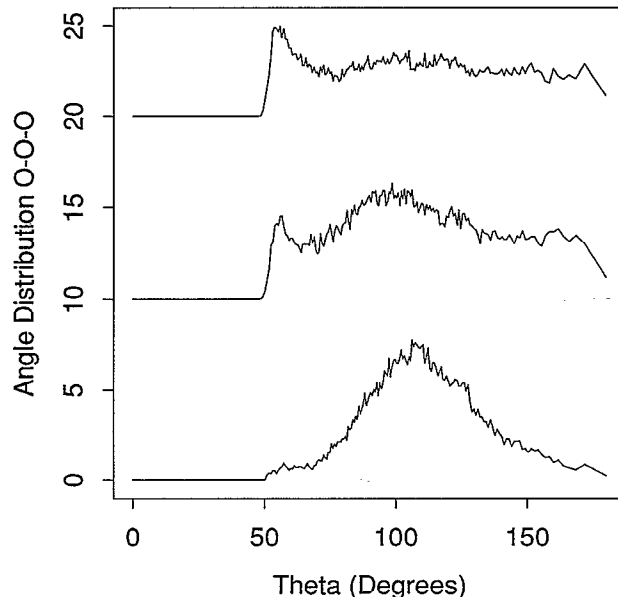
ygens define the triangle, and packing effects where the three water molecules hydrogen-bond to other molecules not in the local complex.

The relative frequency of these types of hydrogen bonding interactions within a local defect as exemplified by Fig. 20 is given in Fig. 21. In Fig. 21 we have evaluated the dot product of the two central oxygen–hydrogen bond vectors with all possible vectors joining the central oxygen with its four, five, and six nearest oxygen neighbors for all
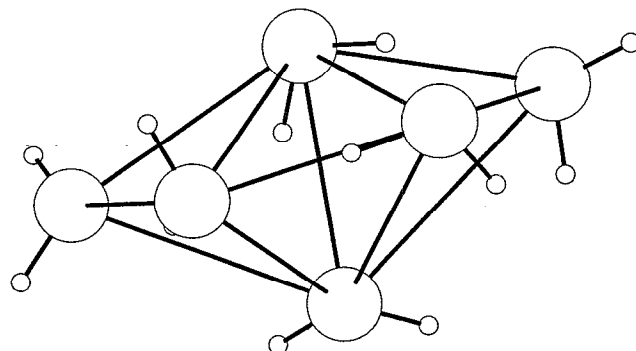

FIG. 20. A representative configuration of a local region of high density (five nearest neighbors about a central water molecule) in the inherent structure of ST4 water simulated at 25 °C and 1 kg/ℓ density. Notice the cluster involves triplets of oxygens arranged in equilateral triangles (solid lines); by sharing vertices and edges, other triplet geometries such as tetrahedral angles are present. The cluster represented here are apparently stabilized by bifurcated hydrogen bonds as well as linear hydrogen bonds.
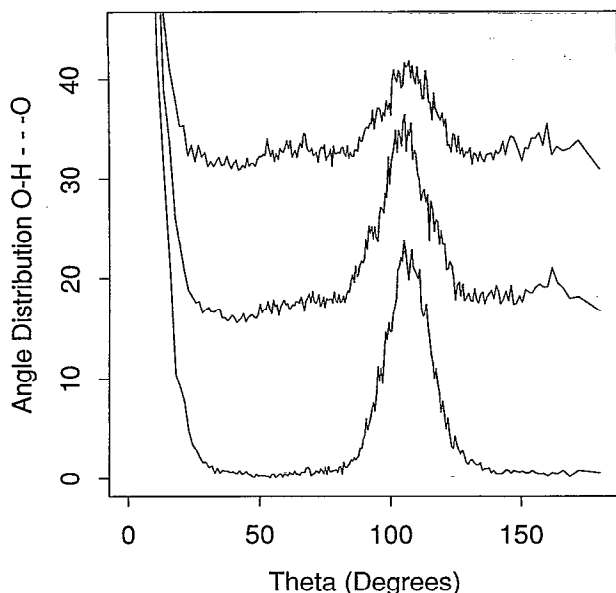
FIG. 21. The O–H···O angle distribution derived from quenched configurations of the ST4 water model simulated at 25 °C and 1 kg/ℓ density, for four (bottom), five (center), and six (top) nearest neighbors only. Geometries corresponding to linear hydrogen bonds ($\sim 0°$), and triplets of oxygens in tetrahedral arrangements where two of the oxygens are hydrogen bonded ($\sim 109.5°$) are easily accommodated in local regions of icelike structure and local regions of high density. Geometries corresponding to bifurcated hydrogen bonds ($\sim 60°$) are virtually nonexistent for four nearest-neighbor densities and are found only in local regions of high density. Bifurcated hydrogen bonds incorporated into such a tetrahedral network may provide the energy lowering of intermediates to aid flow processes in liquid water.

50 inherent structures. The angle distributions which result indicate the occurrence frequency for linear hydrogen bonds ($\sim 0°$) and bifurcated hydrogen bonds ($\sim 60°$). The peak at 109.5° is due to tetrahedral arrangements of three oxygens with one hydrogen bond. It is quite clear that linear hydrogen bonds dominate, although bifurcated bonds are present, as are many other intermediate hydrogen bonding geometries. Nonetheless, these high density clusters seem to be genuine local breakdowns of tetrahedral structure. Because these regions of high density incorporate tetrahedral geometries which can alternate easily between the local defect and surrounding tetrahedral network, the local defects are likely incorporated because they are not too energetically costly, and may well be implicated in flow properties of liquid water.[14] Furthermore, bifurcated hydrogen bonds are also present as a well defined structural entity in our model of water, and may provide confirmation for its assignment in the Raman 3460 cm^{-1} region,[27] assuming they are insensitive to quantal features not explicitly incorporated into our classical model. In addition to verifying the existence of bifurcated hydrogen bonds, Fig. 21 shows that bifurcated hydrogen bonds arise solely as local defects. Whether bifurcated hydrogen bonds are initiators of local defects, or are a result of packing whereby several intersecting solvation shells are required to stabilize their incorporation, remains an open

question until appropriate electronic structure calculations become available.

VII. DISCUSSION AND CONCLUSIONS

This work embodies a novel approach for understanding the role of directional hydrogen bonding for defining the structural and energetic aspects of pure liquid water. A unique statistical mechanical reference potential with no orientational preference was designed to reproduce the short-ranged oxygen order observed from the neutron diffraction[17] experimental $g_{OO}(r)$. To reinsert the appropriate orientational hindrances characterizing hydrogen bonding, we have introduced a new model for fully coupled water which we call ST4. The ST4 model of water provides good descriptions of the pair correlation functions for liquid water, and improved optimum hydrogen bond energy and quadrupole description. Given an isotropic reference fluid and a potential which mimics the orientational anisotropy of liquid water, an investigation of pure water properties and their dependence on directional hydrogen bonding is possible. While we have provided formal perturbation expressions for the thermodynamic energies and pair correlation functions, the influence of directional hydrogen bonding was more fruitfully investigated by Monte Carlo simulation using the perturbation potential defined in Eq. (2.1). A wide variety of energetic and structural properties were evaluated, including two- and three-body correlations, in order to isolate the role of directed hydrogen bonds in determining these quantities.

We have found that maintaining the oxygen–oxygen short ranged order while allowing the hydrogens to rotate freely, characteristics which define our $\lambda = 0$ reference system, results in a fluid which displays a waterlike tetrahedral network, but with a very large number defects (local regions of high density). An examination of the inherent structures derived from $\lambda = 0$ configurations show that these defects can be structurally defined as a complex network of equilateral and near equilateral triangles sharing vertices and edges. These local polyhedral complexes also incorporate triplets of oxygens which are "tetrahedral," as a result of two triangles connected at one vertex rotating in such a way to produce a tetrahedral angle, for example. The reference fluid potential seems to lower the energy of local defects by accommodating some tetrahedral geometries within high density regions, and therefore defects are readily incorporated into the isotropic fluid structure.

Despite an underlying tetrahedral structure which is highly defective in this manner, the reference fluid potential reproduces the experimental $g_{OO}(r)$ for liquid water at 25 °C. One can see then that inverse Monte Carlo procedures,[28] which produce configurations consistent with the pair correlation function(s) of a fluid of interest in order to infer higher order structural correlations, will not necessarily be meaningful. Reproduction of the pair correlation function will not necessarily exhibit the correct three-body correlations, as exemplified by the pair correlation functions and angular distributions of the coupling parameter end points of 0 and 1. This is similar to the situation of devising a charge distribution for a given molecule to re-

produce its observed monopole and dipole values, while grossly misrepresenting the higher order multipoles.

The restoration of directional hydrogen bonding interactions, as introduced by the anisotropic potential in Eq. (1.1), destabilize tetrahedral network defects. However, we have shown that an adequate strength of the anisotropic interactions is necessary in order to relieve the system of the profusion of such defects as exhibited by the $\lambda = 0.00$–0.50 simulations. Nonetheless, some defects remain as is appropriate and consistent with the known properties of liquid water. While the large amount of cohesive energy, and hence high boiling point for such a small molecular weight substance as water is consistent with a strong hydrogen bonding network, energetically accessible local defects are necessary to describe the flow processes[14] of liquid water. In addition, our model of fully coupled liquid water demonstrates the existence of bifurcated hydrogen bonds,[27] and clearly shows that they appear only in local defect regions of high density, i.e., where the number of nearest neighbors for a given central water molecule exceeds four.

We note that we have also evaluated for supercooled water at 198 K the same set of structural probes and inherent structures at the same density discussed in Secs. V and VI, for our $\lambda = 0$ and 1 end points. While we see a sharpening of structural features which are more icelike than the simulations at room temperature, these changes depend only weakly on temperature; this is consistent with the conclusions of Sciortino et al.,[14] where greater structural effects are observed with changes in density.

While this paper has strictly focused on the effect of directional hydrogen bonding on properties of water at 25 °C and a mass density of 1 kg/ℓ, several important future directions are currently forseeable. First, further experimental structural studies which characterize water over a wider range of temperatures and densities will allow the statistical mechanical perturbation approach presented here to extend to these other thermodynamic points of interest, such as the supercooled and/or stretched water regimes. Furthermore, while pure water properties have been investigated in this work, the same anisotropic perturbation formalism and Monte Carlo simulation can be applied to water *solutions*. As a consequence of widespread interest in protein folding where the effect of water is known to be important for describing the folding mechanism and understanding how water stabilizes the folded

state, we will soon report on the perturbation scheme described here, but applied to the hydrophobic interaction. It is interesting to note that Pratt and Chandler's semiempirical theory of the hydrophobic effect[8,9] represents water–water correlations by the experimental $g_{OO}(r)$ correlation function. The present work has revealed that the higher order $(\geqslant 3)$ structural correlations differ substantially between the reference fluid (essentially that used by Pratt and Chandler) and the fully coupled water case. How this difference manifests itself, if at all, in the hydrophobic interaction will be the subject of our companion paper on the effect of orientational anisotropy on water solution properties.

[1] *Water, A Comprehensive Treatise*, edited by F. Franks (Plenum, New York, 1972–1982), Vols. 1–7.
[2] J. E. Del Bene and J. A. Pople, Chem. Phys. Lett. **4**, 426 (1969).
[3] F. H. Stillinger, Science **209**, 451 (1980).
[4] R. A. Kuharski and P. J. Rossky, J. Chem. Phys. **82**, 5164 (1985).
[5] D. Eisenberg and W. Kauzmann, *The Structure and Properties of Water* (Oxford University, London, 1969).
[6] L. Pauling, J. Am. Chem. Soc. **57**, 2680 (1935).
[7] T. Head-Gordon and F. H. Stillinger (to be published).
[8] L. R. Pratt and D. Chandler, J. Chem. Phys. **67**, 3683 (1977).
[9] L. R. Pratt and D. Chandler, J. Chem. Phys. **73**, 3434 (1980).
[10] A. Ben Naim, *Hydrophobic Interactions* (Plenum, New York, 1980).
[11] F. H. Stillinger and A. Rahman, J. Chem. Phys. **60**, 1545 (1974).
[12] N. Metropolis, A. W. Metropolis, M. N. Rosenbluth, A. H. Teller, and E. Teller, J. Chem. Phys. **21**, 1087 (1953).
[13] F. H. Stillinger and T. A. Weber, Science **225**, 983 (1984).
[14] F. Sciortino, A. Geiger, and H. E. Stanley, J. Chem. Phys. **96**, 3857 (1992).
[15] J. P. Hansen and I. R. McDonald, *Theory of Simple Liquids* (Academic, London, 1986).
[16] A. H. Narten and H. A. Levy, J. Chem. Phys. **55**, 2263 (1971).
[17] A. K. Soper and M. G. Phillips, Chem. Phys. **107**, 47 (1986).
[18] K. Watanabe and M. L. Klein, Chem. Phys. **131**, 157 (1989).
[19] R. W. Impey, P. A. Madden, and I. R. McDonald, J. Phys. Chem. **87**, 5071 (1983).
[20] J. K. Percus and G. J. Yevick, Phys. Rev. **110**, 1 (1958).
[21] W. L. Jorgensen, J. Chandrasekhar, J. D. Madura, R. W. Impey, and M. L. Klein, J. Chem. Phys. **79**, 926 (1983).
[22] H. J. Berendsen, J. P. M. Postma, W. F. van Gunsteren, and J. Hermans, in *Intermolecular Forces*, edited by B. Pullman (Reidel, Dordrecht, 1981), p. 331.
[23] D. J. Evans, Mol. Phys. **34**, 317 (1977).
[24] J. Verhoeven and A. Dymanus, J. Chem. Phys. **52**, 3222 (1970).
[25] S. L. Carnie and G. N. Patey, Mol. Phys. **47**, 1129 (1982).
[26] A. Pohorille, L. R. Pratt, R. A. LaViolette, M. A. Wilson, and R. D. MacElroy, J. Chem. Phys. **87**, 6070 (1987).
[27] P. A. Giguère, J. Chem. Phys. **87**, 4835 (1987).
[28] L. Pusztai and G. Tóth, J. Chem. Phys. **94**, 3042 (1991).